


Article

# Measurement-Based Tapped Delay Line Channel Modeling for Fixed-Wing Unmanned Aerial Vehicle Air-to-Ground Communications at S-Band

Yue Lyu <sup>1</sup>, Yuanfeng He <sup>1</sup>, Zhiwei Liang <sup>1</sup>, Wei Wang <sup>1,\*</sup> , Junyi Yu <sup>2</sup> and Dan Shi <sup>3</sup>

<sup>1</sup> School of Information Engineering, Chang'an University, Xi'an 710064, China; 2020024004@chd.edu.cn (Y.L.); 2022124024@chd.edu.cn (Y.H.); 2023024023@chd.edu.cn (Z.L.)

<sup>2</sup> Beijing Metaradio Technologies Co., Ltd., Beijing 100070, China; junyi.yu@metaradio.tech

<sup>3</sup> School of Electronic Engineering, Beijing University of Posts and Telecommunications, Beijing 100876, China; shidan@bupt.edu.cn

\* Correspondence: wei.wang@chd.edu.cn

**Abstract:** Fixed-wing unmanned aerial vehicles (UAVs) are widely considered as a vital candidate of aerial base station in beyond Fifth Generation (B5G) systems. Accurate knowledge of air-to-ground (A2G) wireless propagation is important for A2G communication system development and testing where, however, there is still a lack of A2G wideband channel models for such a purpose. In this paper, we present a wideband fixed-wing UAV-based A2G channel measurement campaign at 2.7 GHz, and consider typical flight phases, based on which a wide-sense stationary uncorrelated scattering (WSSUS)-based tapped delay line (TDL) wideband channel model is proposed. Parameters of individual channel taps are analyzed in terms of gain, amplitude distribution, Rice factor and delay-Doppler spectrum. It is shown that UAV flight phases significantly influence the channel tap parameters. Particularly, the “Bell”-type spectrum is found to be the most suitable model for the delay-Doppler spectrum under various flight scenarios for A2G propagation. The proposed channel model can provide valuable assistance and guidance for UAV communication system evaluation and network planning.

**Keywords:** air-to-ground communication; channel measurement and modeling; delay-Doppler spectrum; tapped delay line model



**Citation:** Lyu, Y.; He, Y.; Liang, Z.; Wang, W.; Yu, J.; Shi, D. Measurement-Based Tapped Delay Line Channel Modeling for Fixed-Wing Unmanned Aerial Vehicle Air-to-Ground Communications at S-Band. *Drones* **2024**, *8*, 492. <https://doi.org/10.3390/drones8090492>

Academic Editor: Emmanouel T. Michailidis

Received: 27 July 2024

Revised: 4 September 2024

Accepted: 15 September 2024

Published: 17 September 2024



**Copyright:** © 2024 by the authors. Licensee MDPI, Basel, Switzerland. This article is an open access article distributed under the terms and conditions of the Creative Commons Attribution (CC BY) license (<https://creativecommons.org/licenses/by/4.0/>).

## 1. Introduction

Over the past two decades, air-to-ground (A2G) communications, particularly between unmanned aerial vehicle (UAV) and ground systems, have received considerable attention. Compared to terrestrial base stations, A2G communications via UAVs offer flexible deployment and extended coverage, as UAV-based aerial base stations can be promptly deployed to regions that terrestrial base stations may not be able to cover. Particularly, the fixed-wing UAV has longer flight endurance and larger overload that enables coverage enhancement and network optimization of terrestrial-based communication systems [1]. As such, UAV has been widely considered as a vital platform for aerial base stations in beyond Fifth Generation (B5G) communication [2,3].

Commercial technologies such as Fourth Generation (4G) Long Term Evolution (LTE), Fifth-Generation NewRadio 5G NR, Wi-Fi, and millimeter wave are capable of supporting the A2G communication link transmission. For instance, Wi-Fi 5 (802.11ac) and Wi-Fi 6 (802.11ax) can provide convenient and high-speed connection options for UAV operations and data transmission over short distances. Additionally, organizations such as the International Telecommunication Union (ITU), Unmanned Aircraft Systems International Association (UASIA), and the Federal Aviation Administration (FAA) in the United States have initiated multiple research projects to establish international standards and

regulations for UAV communications. These standards and regulations primarily address the communication technologies, protocols, and spectrum usage of UAVs. Particularly, the frequency band allocated to A2G communications varies by countries and regions, where the band at 2.4 GHz is widely adopted for remote control and data transmission in small-sized UAVs. Other frequency bands, such as L- and C-bands, are also considered in A2G communication for specific demands.

Accurate knowledge on the A2G wireless channel is of great importance to facilitate the development of UAV-based A2G communications [4,5]. It is vital to extensively conduct channel measurement campaign and develop a wideband A2G channel model to promise an accurate simulation of A2G communication. A comprehensive literature review and analysis of existing A2G channel measurements and modeling of UAV have been provided in [1,2,5–9]. In our previous works, we conducted rotary-wing UAV-based A2G channel measurements at 2.4 GHz, 5.9 GHz, and ultra-wideband frequency band [10–12]. In [13], the fading characteristics of A2G, channel in different frequency bands are considered and analyzed, based on which a novel autocorrelation model of shadowing is proposed. Matolak et al. [14] focus on the fuselage shadowing characteristics of an A2G channel through measurements, and found that placing multiple antennas on a UAV can mitigate shadowing. The authors of [15] analyze the propagation characteristics at different flight attitudes for both line-of-sight (LoS) and obstructed-LoS (OLOs) conditions and propose a new path loss model.

As for the studies of wideband channel, the authors of [16] evaluate the Rice factor and root mean square delay spread (RMS-DS) of A2G channel with a bandwidth of 500 MHz. There are other studies on A2G propagation channels based on a wideband channel measurement campaign, as reported in [17,18]. The authors of [19] propose a geometry-based stochastic channel model in an airport environment. In [20–22], a tapped delay line (TDL) model is presented for hilly, suburban, and over-water scenarios, where parameters like the probability of occurrence, relative power, phase, duration of individual multi-path component (MPC) are considered. The authors of [23] evaluate the propagation characteristics, in which model planes is fixed in order to simulate inter UAV communication scenario. In this work, a TDL channel model is proposed considering the real motion trajectories of the UAV.

As described in previous paragraphs, extensive research has been conducted on low altitudes (below 120 m). However, there are very few reported works with focus on fixed-wing UAV-based A2G channels at altitudes above 200 m, at which an aerial base station is usually operated. A comprehensive wideband A2G channel model, which incorporates both measurement-based statistic evidences and temporal evolution of channel [24], is still missing. Particularly, it is essential to accurately model the A2G channel at potential frequency bands of B5G for fixed-wing UAVs in remote areas, like rural environments, in order to boost the development of future communication networks and coverage performance. Therefore, by considering the limitations of previous studies, we conducted a fixed-wing A2G channel measurement campaign, based on which the wideband propagation characteristics at different UAV flight attitudes are investigated, and a Wide-Sense Stationary Uncorrelated Scattering (WSSUS)-based TDL channel model is proposed. The main contributions of the paper are summarized as follows:

- We present a fixed-wing UAV A2G channel measurement campaign at 2.7 GHz with 25 MHz bandwidth in a rural area, based on a developed channel sounding system consisting of vector signal transceiver and software radio device. The measurement was with emphasis on four typical UAV flight phases, and different flight altitudes (up to 700 m), velocities, and transmitter–receiver distances.
- We propose to model the A2G channel with a WSSUS-based complete TDL channel model, with a typical system bandwidth of 20 MHz for A2G applications. The average power, short term evolution of complex amplitude, and delay-Doppler spectrum of individual channel taps are considered in the proposed model.

- Based on the measurement data, we comprehensively analyze the characteristics of the propagation channel. The proposed TDL channel model is parameterized based on the measurement data in terms of number of taps, averaged power delay profile (PDP), phase, fading distribution, Rice factor, and delay-Doppler spectrum of each channel tap. Four types of spectral models are considered to analyze delay-Doppler spectrum of individual tap.

The remainder of this paper is structured as follows. The A2G measurement campaign is addressed in Section 2. The proposed TDL model is presented in Section 3. Analysis and results of the TDL channel model-based A2G measurement data are given in Section 4. Finally, the conclusions are drawn in Section 5.

## 2. A2G Channel Measurement Campaign

### 2.1. Measurement Equipment

In this section, we present the A2G channel sounding measurements for the fixed-wing vertical takeoff and landing (VTOL) UAV conducted in rural area of Zigong, China. The transmitter system consists of a high performance Universal Software Radio Peripheral (USRP) Ettus X310, an on-board computer controlling the USRP, a rubidium clock, an Inertial Measurement Unit (IMU) navigation system recording the coordinates and UAV attitude, a power amplifier (PA) accompanied with a bandpass filter, and an omni-directional antenna. The transmitter mounted on the UAV emits a 36 dBm sounding signal with rectangular shaped spectrum periodically with bandwidth of  $B = 25$  MHz at 2.7 GHz. An IMU navigation system with centimeter-level positioning accuracy was used to record the position and attitude of UAV. The omni-directional transmitter antenna was fixed below the airframe to minimize interference of the fuselage on the signal.

The ground receiver system consists of the NI vector signal transceiver PXIe-5841 controlled by PXIe-8861 via LabVIEW, a low-noise amplifier (LNA), a rubidium clock, a high accuracy global navigation satellite system (GNSS) receiver, and an omni-directional antenna. A GNSS receiver with sub-meter accuracy was used to record the position of the receive antenna, which was approximately 1.5 m above the ground as visualized in Figure 1.

The same type of rubidium clocks providing high precision 10 MHz frequency standards to all relevant radio devices for synchronization. Before the channel measurement, both clocks were pre-adjusted in order to synchronize frequency offset between two clocks. Further, a calibration of all used front-end including radio devices and cables was performed by directly connecting transmitter and receiver in order to mitigate the front-end effect. The channel measurement parameters are listed in Table 1.

**Table 1.** Channel measurement parameter.

Parameter	Value
Carrier frequency $f_c$	2.7 GHz
Bandwidth	25 MHz
Number of sub-carriers $N$	512
Transmit power	$\sim 36$ dBm
OFDM signal period	20.48 $\mu$ s
Measurement time grid	1.024 ms
Transmitter antenna	Omni-directional, 6 dBi (V-pol.)
Receiver antenna	Omni-directional, 3 dBi (V-pol.)
UAV speeds	27 m/s
UAV maximum altitude	700 m
UAV maximum distance	3 km

The signals acquired during the measurements were processed using MATLAB software 2023(b) to extract the frequency domain channel transfer function. channel impulse response (CIR) was obtained by inverse Fourier transform of the frequency response by using the window function to reduce impact of the sidelobe of the effect. Through the

channel measurement campaign, a total number of 2,800,000 CIR snapshots were collected, covering different UAV flight phases.

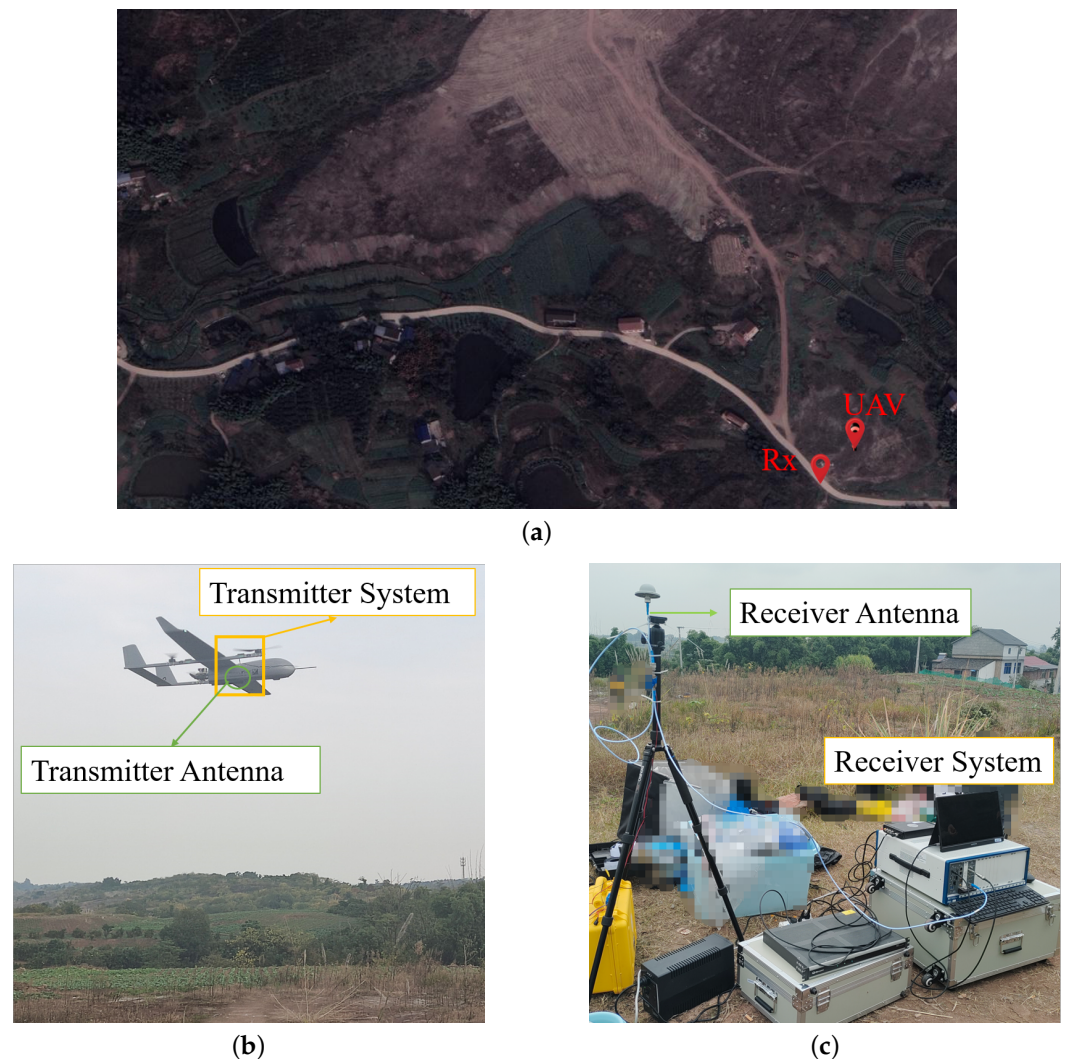


**Figure 1.** (a) Measurement scenarios, with the UAV's take off point and the ground reception point marked in the figure. (b) The UAV is equipped with transmitter system and antenna as the air terminal. (c) Ground receiver system and antenna.

### 2.2. Measurement Scenarios

The measurements were taken in a typical rural area in China, which primarily consist of vegetation, farmlands, and residential houses, as depicted in Figure 1a. The receiver was placed approximately 35 m away from the UAV's takeoff point in an open area without any obstructions. The UAV flew along a predefined trajectory, with a constant speed of 27 m/s and a maximum transmitter-receiver (Tx-Rx) distance of 3 km. The maximum flight height was 800 m and the flight duration was approximately 2 h. As noted, a strong LoS component is observed for the most time in our A2G measurement.

### 2.3. Typical UAV Flight Phases

The fixed-wing VTOL UAV is featured with the characteristics of both fixed- and rotary-wing UAV, which is capable of taking-off and landing without long runway. As a result, it is suitable for in complex and irregular terrains such as urban operations or rural areas. This kind of UAV can carry heavier payloads and has the capability of high-speed flight; therefore, it can accommodate more sensors and communication equipment at high UAV altitudes.

Thus, as shown in Figure 2, we consider different flight operational stages of the UAV to analyze the propagation characteristics of the A2G channel, which are specifically divided into the four stages:

- Vertical takeoff and landing: the UAV activates its rotors and increases the rotary speed, enabling the UAV take-off or land vertically.
- Departure and approach at low altitude: the UAV switches to fix-wing flight mode, where the speed and altitude steady increase.
- Hovering preparation: the UAV ascends in a circular path with a radius of 300 m up to 300 m height, flying at a constant speed about 27 m/s.
- Steady flight at various altitudes: The UAV maintains straight-line flight at heights of 300 m, 500 m and 800 m. Noting that, the UAV always flight along the same route at all three altitudes.

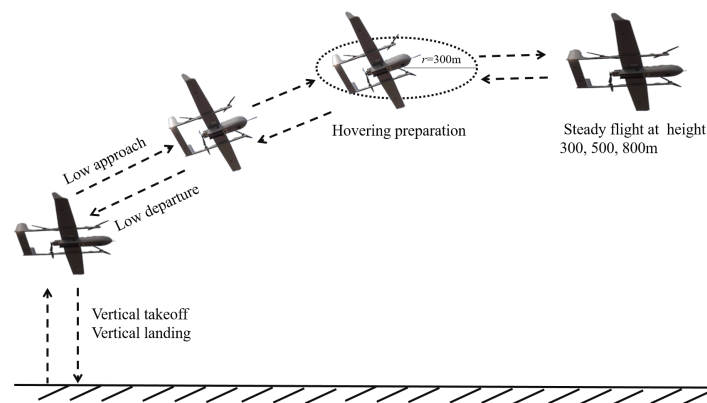


**Figure 2.** Typical flight phases of VTOL UAV communications.

Considering that UAVs have similar channel propagation characteristics for vertical takeoff or landing and for low departure or approaches, we only analyze one of these conditions. Finally, by combining different UAV heights and Tx-Rx distances, we consider six flight scenarios, marked as FS1 to FS6. Detailed measurement parameters of different flight stages are listed in Table 2.

**Table 2.** Detailed measurement parameters of different flight stages.

Mark	Flight Phase	Height	Speed	Distance
FS1	Vertical landing	0–40 m	1.2 m/s	35–60 m
FS2	Low approach	40–100 m	1.2–27 m/s	70–300 m
FS3	Hover preparation	100–300 m	27 m/s	400–600 m
FS4	Steady flight	300 m	27 m/s	1690–2160 m
FS5	Steady flight	500 m	27 m/s	1740–2170 m
FS6	Steady flight	800 m	27 m/s	1750–2170 m

### 3. Tapped Delay Line Model

Modeling the propagation channel is one of the most challenging tasks in the design of wireless communication systems, especially for A2G scenarios, where special requirements on channel measurement requirements are addressed. Let us first consider a typical orthogonal frequency division multiplexing (OFDM) symbol duration (i.e., 66.67  $\mu$ s) in Fifth Generation (5G) NR, and a typical UAV flight speed of 100 km/h. In compliance with the 5G NR standard,  $B_e = 20$  MHz bandwidth was used for subsequent analysis and modeling, i.e., the delay bin is  $\frac{1}{B_e}$ . Within on data symbol duration, the maximum movement of antenna is 0.002 m, which has negligible impact on large scale parameters of the channel. Therefore, we present the A2G TDL channel model for communication applications based on the WSSUS assumption.

Based on the WSSUS assumption, the channel can be simplified such that the complexity of the model is low where the CIR is easily to simulate and the important stochastic characteristics of the channel are kept. However, the WSSUS assumption is often invalid in realistic environments, depending on different application scenarios. For instance, positioning applications require accurate time evolution of the channel path parameters in order to ensure an accurate simulation environment for positioning algorithm tests. Therefore, the WSSUS assumption is not valid anymore. A more popular approach, i.e., a geometry-based stochastic channel model (GSCM), has attracted more attention with more accurate simulated CIR, but also with higher complexity in both modeling and parameter extraction. Nevertheless, in this paper, the tap delay line channel model is sufficient for communication purposes.

### 3.1. Representation of Channel Impulse Response

The received signal is consists of a certain number of replications of transmitted signal propagated via different propagation paths. The baseband impulse response of a multipath channel can be expressed as [25]

$$h(t, \tau) = \sum_{i=0}^{N(t)-1} a_i(t) e^{j\phi_i} e^{j2\pi f_i(t)t} \delta(\tau - \tau_i(t)), \quad (1)$$

where  $t$  and  $\tau$  are time and delay, respectively. The terms  $a_i(t)$ ,  $\tau_i(t)$ , and  $f_i(t)$  are the magnitude, delay, and Doppler shift of the  $i$ th MPC at time  $t$ .  $\phi_i$  is the initial phase of the  $i$ th path.  $N(t)$  is the total number of MPCs at time  $t$ .  $\delta(\cdot)$  represents the Dirac-delta function, which describes the specific time of arrival  $\tau_i$  of individual MPC at time  $t$ .  $f_i(t)$  represents the Doppler shift that is mainly caused by the movement of transmit and/or receive antennas. The Doppler shift frequency depends on relative moving speed  $\Delta v(t)$  of antennas, the wavelength, and the angle of arrival  $\gamma_i(t)$  of the microwave, and can be expressed as [25]

$$f(t) = -\frac{\Delta v(t)}{\lambda} \cdot \cos(\gamma_i(t)), \quad (2)$$

where  $\Delta v(t)$  represents the relative speed,  $\lambda$  is the wavelength calculated according to the carrier frequency  $f_c$  and the speed of light  $c$ . Therefore, the maximum Doppler frequency value can be calculated based on geometric relationship when  $\cos(\gamma(t)) = 1$ . In addition,  $\gamma_i(t)$  includes the arrival direction and the movement direction, which determines the power spectral density or Doppler spectrum of  $\gamma_i(t, \tau)$  [26].

In A2G communications, the received signal at the ground is distorted due to multipath propagation and blockage by ground objects. Considering the fact that the UAV was moving at a constant speed, we assume that the fading process is stationary over a relatively short period of time, i.e., in which the WSSUS assumption is valid. Thus, the scatters at different time delays are uncorrelated, and only depend on frequency separation, and different Doppler shifts are uncorrelated depending only on time differences [24]. A reasonable time window shall be selected, where a large window could cause non-stationary characteristics and an “averaged” Doppler spectrum, whereas a small window could result in low resolution in Doppler spectrum. As reported by [27,28], the stationary time can be calculated as  $t_s = d_s / \Delta v$ , where  $d_s$  represents the stationary distance in the range between  $20\lambda$  to  $40\lambda$  and  $\Delta v$  is the relative speed between transmitter and receiver. In this paper, we determine individual stationary time window lengths for different scenarios at various flight stages of the UAV to ensure a reliable analysis of the data.

### 3.2. A2G TDL Model

As one of the most popular implementations of the WSSUS channel, the TDL model is adopted to simulate the A2G propagation channel, where the complex amplitude of individual channel taps varies over time [24]. The TDL channel model is a classical “block fading” model for efficient simulations in communication applications, like the COST-207 model. Thus, the CIR can be represented as

$$h(t, \tau) = \sum_{i=1}^M c_i(t) \delta(\tau - \tau_i), \tag{3}$$

where  $M$  is number of taps (to distinguish from the true number of paths  $N(t)$ , we use  $M$  to denote the number of taps, which is a constant value within a given scenario),  $c_i(t)$  is the complex coefficient of the  $i$ th tap depending on time, and  $\tau_i$  is the delay of the  $i$ th tap. For a WSSUS channel, wide-sense stationary implies that large scale characteristics of the channel are rather constant over the considered time duration and the complex coefficient of the individual tap is generated independently. Figure 3 shows a simple representation of the TDL model. The number of taps depends on the dedicate system bandwidth and maximum propagation delay. The time variation of the complex channel tap is described by short-term fading process and Doppler spectrum [29]. In the following, we describe the model characteristics of a certain number of taps, such as the delay, amplitude distribution, K-factor and Doppler spectrum of individual taps, and the statistical channel model.

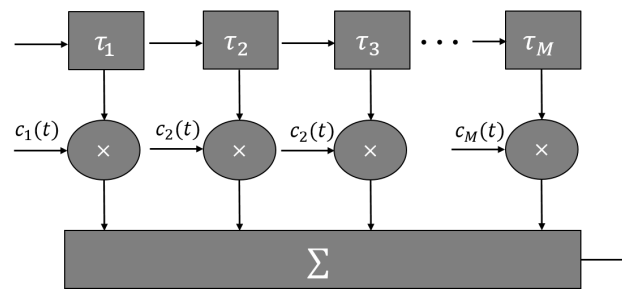


Figure 3. Representation of a TDL model.

### 3.2.1. Average Power Delay Profile, Delay and Power Value

Due to the system bandwidth, the observable delay resolution of MPCs is limited. The average power delay profile (APDP) can be calculated as [29]

$$P(n\Delta\tau) = \frac{1}{Q} \sum_{q=0}^{Q-1} |[h^*(n\Delta\tau, q\Delta t)]|^2, 0 \leq n \leq N - 1, \tag{4}$$

where  $q = 0, \dots, Q - 1$  is the time index of measured CIR in a local area. To calculate the APDP for communication application, the CIR shall be normalized in both delay and power domains. The term  $h^*$  is the CIR normalized in power by the total received power, and in delay by the LoS [25].  $q\Delta t$  is the observation instant of the  $q$ th CIR.  $\Delta\tau$  is delay resolution, which equals to  $\Delta\tau = 1/W$ , where  $W$  is the measurement bandwidth.  $n$  is delay tap index, and  $N$  is the maximum number of CIR samples from the measurement. In the channel model, the number of taps  $M$  is determined with the tap index  $m = 1, \dots, M$ , which depends on the bandwidth of wireless radio system and threshold  $\beta_m$ , and the channel tap samples with power values below the threshold is set to zero [30]. In the following, the average delay and power of the  $m$ th taps are given by

$$\tau_m = \frac{\sum_{n=i_m}^{i_m+b-1} n\Delta\tau \cdot P(n\Delta\tau)}{\sum_{n=i_m}^{i_m+b-1} P(n\Delta\tau)}, \tag{5}$$

$$a_m = \frac{1}{b} \sum_{n=i_m}^{i_m+b-1} |h^*(n\Delta\tau, q\Delta t)|^2, \tag{6}$$

where  $i_m$  is the sample number start of each group, where  $i_1$  is the first nonzero sample after applying the threshold [31]. The variable  $b$  represents samples which are calculated by the obtained  $L$  samples divided into  $M$  groups.

Figure 4 visualizes an example of the APDP normalized both in delay and in power. It is worth noting that the CIR samples are discarded if the corresponding normalized power

is 25 dB below relative to the strongest path. The  $x$ - and  $y$ -coordinates are corresponding to the normalized delay and power of individual tap, respectively.

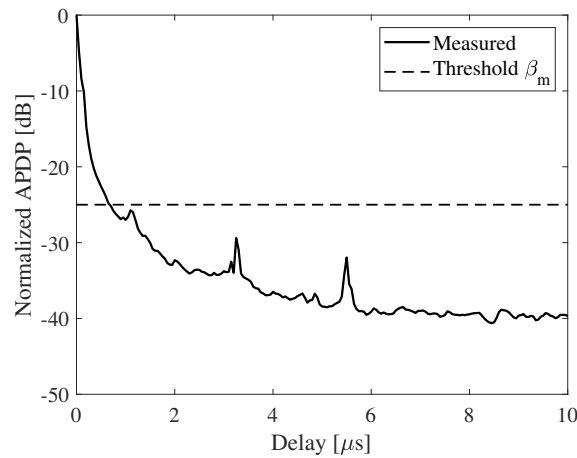


**Figure 4.** An example of normalized APDP.

### 3.2.2. Amplitude Fading

To accurately understand and model the power variations characteristics of individual channel taps, the amplitude distribution of taps are evaluated. Depending on the feature of radio propagation channels, different modeling approaches are used to represent the statistical fading behavior of the envelope amplitude [32]. To mitigate the fast fading effect, CIRs are usually averaged over a certain measurement duration. In this work, we use the window length of 100 wavelengths to average the CIRs according to the speed of UAV during the measurement.

Assuming that the distance between transmitter and receiver is sufficiently large, all received signals belong to the same channel tap are plane waves without a dominant component. As a result, the amplitude of the channel tap generally follows the Rayleigh distribution, and the gain of the tap can be modeled as a zero mean Gaussian random variable [33]. The probability density function (PDF) of Rayleigh distribution is given as

$$p_f(|\alpha|, \sigma_l) = \frac{|\alpha|}{\sigma_l^2} e^{-\frac{|\alpha|^2}{2\sigma_l^2}}, \quad (7)$$

where  $\sigma_l$  is the standard deviation.  $|\alpha|$  is the normalized magnitude, which is given by

$$\alpha(n\Delta t, (m-1)\Delta\tau) = \frac{h^*(n\Delta t, (m-1)\Delta\tau)}{\sqrt{P((m-1)\Delta\tau)}}. \quad (8)$$

When a dominant path or LoS component is present, the amplitude distribution of the taps can be modeled by Rice distribution; the PDF of the Rice distribution is [34]

$$p_f(|\alpha|, K_r, \Omega_r) = \frac{1 + K_r}{\Omega_r} I_0 \left( 2\sqrt{\frac{K_r(K_r + 1)|\alpha|}{\Omega_r}} \right) \exp \left( -\frac{K_r\Omega_r - (K_r + 1)|\alpha|}{\Omega_r} \right), \quad (9)$$

where  $K_r$  denotes the K-factor corresponding to the power ratio between the LoS component and other MPCs.  $I_0(\cdot)$  is the modified Bessel function, and  $\Omega_r$  is the sum of the power of these two kinds of path. The stronger the LoS component is, the less likely the deep fading occurs. The K-factor reflects the power ratio between the dominant path and the scattering path in multipath propagation, which directly affects signal quality, the design of equalization and detection algorithms, and the choice of modulation and coding schemes, as well as linking budget and power control strategies. The design of UAV communication



system needs to be adjusted according to the K-factor in the actual environment to ensure system stability and efficiency. The value of the Rice K-factor is calculated using the method of the moment [35].

Other typical distributions used to describe the amplitude are Gaussian distribution, Weibull distribution [36], Nakagami distribution, which are given as [32]:

- Gaussian distribution:

$$p_f(|\alpha|, \mu_g, \sigma_g) = \frac{1}{\sigma_g \sqrt{2\pi}} \exp\left(-\frac{(|\alpha| - \mu_g)^2}{2\sigma_g^2}\right), \quad (10)$$

where  $\mu_g$  and  $\sigma_g$  denote the mean and standard deviation of the distribution, respectively.

- Weibull distribution:

$$p_f(|\alpha|, \beta_w, \Omega_w) = \frac{\beta_w}{\Omega_w} |\alpha|^{\beta_w-1} \exp\left(-\frac{|\alpha|^{\beta_w}}{\Omega_w}\right), \quad (11)$$

where  $\Omega_w$  and  $\beta_w$  denote the shape parameter and scale parameter, respectively.

- Nakagami distribution:

$$p_f(|\alpha|, \varphi, \Omega) = \frac{2\varphi^\varphi}{\Gamma(\varphi)\Omega^\varphi} |\alpha|^{2\varphi-1} \exp\left(-\frac{\varphi}{\Omega} |\alpha|^2\right), \quad (12)$$

where  $\varphi$  and  $\Omega$  denote the shape and spread parameter, respectively.  $\Gamma(\varphi)$  is the Gamma function evaluated at  $\varphi$ .

### 3.2.3. Doppler Spectrum per Tap

The individual channel tap corresponds to the superposition of several physical propagation paths that arrive at the receiver within one delay bin. Therefore, each channel tap experiences the “narrowband” characteristics, among which the Doppler spectrum of each tap is one important feature in the modeling. The Doppler spectrum of each tap maybe time variant or invariant. The Doppler spectrum strongly depends on the propagation environment, as well as the tap delay.

The Doppler spectrum of individual channel taps can be modeled by accurate calculation based on geometry of transmitter, receiver and scatterers. The authors of [37,38] present a theoretical analysis on Doppler PDF to describe any time-variant, single-bounce, mobile-to-mobile scattering channel. In such kinds of approaches, the scatterer plane and the antennas velocities are considered in order to derive the joint Doppler PDF. In contrast, the simpler statistical approach to model Doppler spectrum of individual channel tap is to use specific function that fits the best to the observed Doppler spectrum. The typical Doppler spectrum function of the tap includes the flat, Jake, Bell, and Gaussian spectra. The Jake spectrum, also known as the U-shape spectrum, is well recognized as a result of isotropic and uniformly distributed scatters. In contrast, the Bell and Gaussian spectra are typically for non-isotropic scatters that are closely located, resulting in dense multipath propagation with similar propagation delays and angles of arrival. The analytical expressions of all simulated Doppler spectra and the used model selection criteria are presented in Appendix A.

## 4. Parameterization and Analysis of the Proposed TDL Model

In this section, the procedure shown in the previous subsections is applied to six different propagation channels, denoted as FS1 to FS6. The obtained results of the proposed TDL model are shown and analyzed based on the measurement data collected, as described in Section 2.

#### 4.1. Average PDP and Tap Characteristics

As described above, we calculated the APDP, where the PDF of the obtained APDP for the low approach scenario is visualized in Figure 5a. The power loss at delay 0 ns should be around 0 dB for the LoS path. Additionally, the APDP can be approximated as a unilateral exponential function, which decreases exponentially with the delay [24]. The normalized APDP is shown in Figure 5b, where the number of extracted effective taps  $M = 10$  with the given threshold of 25 dB below the strongest tap power. The power threshold is a model empirical value, which is given to determine the number of taps, and excess delay of individual taps with respect to the LoS path for all measurement scenarios as summarized in Table 3.

**Table 3.** Channel parameters of proposed TDL model for FS1 to FS6: delay, amplitude, K-factor and fading distribution for per tap.

Taps	FS1				FS2			
	$\tau_m$ (ns)	$a_m$ (dB)	$k_m$ (dB)	Fading Distribution	$\tau_m$ (ns)	$a_m$ (dB)	$k_m$ (dB)	Fading Distribution
1	0	0	27.58	Rice	0	0	19.78	Weibull
2	50	-5.969	11.89	Normal	50	-5.609	7.609	Weibull
3	100	-11.91	8.412	Normal	100	-9.801	6.526	Normal
4	150	-13.99	7.784	Normal	150	-12.61	5.974	Normal
5	200	-18.62	9.531	Normal	200	-16.64	4.889	Normal
6	250	-20.82	8.476	Normal	250	-19.00	6.674	Normal
7	300	-21.95	8.438	Normal	300	-20.75	7.375	Normal
8	350	-23.38	7.428	Normal	350	-22.07	7.236	Normal
9	400	-23.95	7.045	Normal	400	-23.23	7.318	Normal
10					450	-24.33	7.363	Normal
Taps	FS3				FS4			
	$\tau_m$ (ns)	$a_m$ (dB)	$k_m$ (dB)	Fading Distribution	$\tau_m$ (ns)	$a_m$ (dB)	$k_m$ (dB)	Fading Distribution
1	0	0	20.03	Rice	0	0	15.96	Weibull
2	50	-4.789	8.905	Weibull	50	-5.595	6.375	Normal
3	100	-8.425	8.679	Weibull	100	-10.02	2.746	Rice
4	150	-10.16	3.404	Nakagami	150	-12.88	-1.846	Nakagami
5	200	-14.72	6.387	Normal	200	-16.88	0.953	Normal
6	250	-17.13	7.760	Normal	250	-18.98	2.481	Normal
7	300	-18.89	7.596	Normal	300	-20.61	3.314	Normal
8	350	-20.17	7.353	Normal	350	-21.81	3.395	Normal
9	400	-21.13	6.800	Normal	400	-22.96	3.598	Normal
10	450	-21.86	6.508	Normal	450	-23.86	3.602	Normal
11	500	-22.59	6.388	Normal	500	-24.57	3.792	Normal
12	550	-23.24	5.747	Normal				
13	600	-23.97	5.399	Normal				
14	650	-24.81	5.136	Normal				
Taps	FS5				FS6			
	$\tau_m$ (ns)	$a_m$ (dB)	$k_m$ (dB)	Fading Distribution	$\tau_m$ (ns)	$a_m$ (dB)	$k_m$ (dB)	Fading Distribution
1	0	0	17.08	Weibull	0	0	17.23	Weibull
2	50	-5.478	7.094	Normal	50	-5.600	6.079	Normal
3	100	-10.06	3.857	Rice	100	-10.35	3.925	Normal
4	150	-13.05	2.610	Normal	150	-12.77	2.203	Normal
5	200	-16.93	2.075	Normal	200	-16.78	2.164	Normal
6	250	-19.10	3.952	Normal	250	-19.01	3.798	Normal
7	300	-20.83	4.471	Normal	300	-20.68	4.496	Normal
8	350	-22.13	4.305	Normal	350	-22.04	4.417	Normal
9	400	-23.21	4.540	Normal	400	-23.15	4.535	Normal
10	450	-24.11	4.522	Normal	450	-24.10	4.436	Normal
11	500	-24.54	4.244	Normal	500	-24.86	4.522	Normal

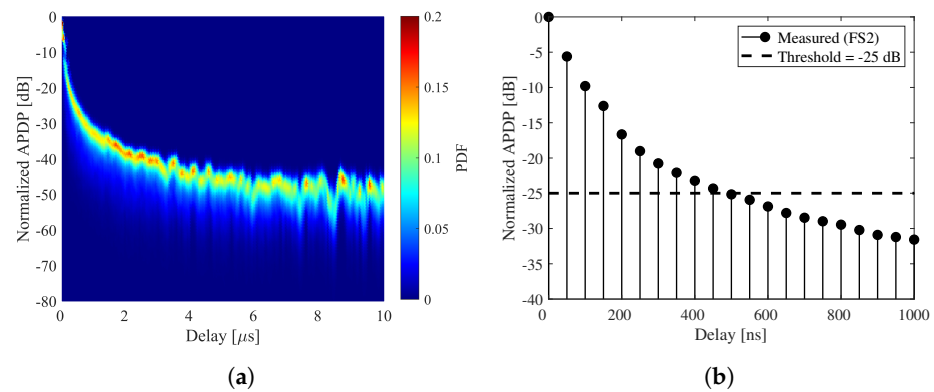


**Figure 5.** (a) The measured PDF of normalized empirical APDP. (b) The normalized empirical APDP for FS2 model.

In our observations, the maximum number of tap in FS1 is the smallest among all six considered scenarios, where  $\tau_{max} = 400$  ns and  $\tau_{max} = \tau_M - \tau_1$ . The maximum number of resolvable taps is 14 in FS3, whereas the delay and tap numbers are the same for scenarios FS4 to FS6. Variables including UAV speed, UAV altitude and Tx-Rx distance may cause significant differences in parameters (e.g., number of taps  $M$ , tap power  $a_m$ , and tap delay  $\tau_m$ ) and, therefore, shall be considered in the model.

As one important characteristic of propagation channel, the Doppler shift depends on the UAV speed and wave direction. Further, the Doppler spread and its spectrum shape indicate the scatterer properties. In scenarios FS4 to FS6, the same number of taps, tap power, and tap delay are obtained at different altitudes, and similar parameter variation trends are observed. Thus, we conclude that the impact of UAV altitude on the TDL model is relatively small if the UAV speed and Tx-Rx distance are fixed.

#### 4.2. Fading Statistics and K-Factor Values of Individual Tap

Based on the measurement result, different fading behavior is observed for different channel taps. It is important to evaluate the statistical characteristics of individual channel taps, where we consider five typical candidate distributions (Normal, Weibull, Rice, Rayleigh, and Nakagami distribution). To quantitatively analyze the accuracy of five distributions, we utilize the Cramér–von Mises (CVM) test as the goodness-of-fit index, which is more robust and accurate than popularly used Kolmogorov–Smirnov (KS) test. It is an enhanced method due to the integration of the power of the difference between the cumulative distribution functions (CDFs) of measurement data and of the theoretical distribution [39]. The goodness-of-fit index of CVM test can be calculated as [34]

$$\rho_c = \int_{-\infty}^{+\infty} |F_x(x) - F(x)|^2 dF(x), \quad (13)$$

where  $F_x(x)$  and  $F(x)$  are the empirical and theoretical CDF of the sample  $x$ , respectively. We statistically analyze the amplitude distribution and calculate the Rice K-factor of per tap, the suitable distribution and K-factor values  $K_m$  can be shown in Table 3.

In scenario FS1, where the UAV is vertically landing, the envelope of the first tap follows the Rice distribution according to the goodness-of-fit index of CVM test, with the maximum K-factor value of individual channel taps is 27.58 dB. This finding is also consistent with physical reality, where a strong LoS component is usually present within the first channel tap. In scenario FS1, other channel taps are found to follow the normal distribution, which usually implies a large value of the K-factor. This is attributed to the UAV descending smoothly at a speed of 1.2 m/s, in the open rural environment, resulting in less severe multipath effect. Therefore, for UAVs in low-altitude scenarios, high K-factor values are conducive to improving signal quality, simplifying equalization and

detection algorithms in UAVs communication systems, and allowing the use of higher-order modulation schemes to support higher data transfer rates and bandwidth utilization.

In the scenario FS2, the first two channel taps are found to follow the Weibull distribution, where the estimated scale and shape parameters are  $\beta_{w1} = 18.72$ ,  $\Omega_{w1} = 1.015$ , and  $\beta_{w2} = 3.813$ ,  $\Omega_{w2} = 0.998$  for the first and the second taps, respectively. It can be seen that the parameter  $\beta_m$  of the first tap are much larger than that of the second tap, and the other taps all submit to normal distribution. In the scenario FS3, when the UAV is preparing for circling, the altitude of the UAV steady increases resulting in a significant change terrain environment. Objects on ground like houses and trees may cause MPCs, and can be observed clearly in the first four taps, which are found to follow Rice, Weibull, Weibull, and Nakagami distributions, respectively.

In measurement scenarios from FS4 to FS6, we evaluate the impact of different UAV altitude on the proposed channel model. It is observed that the K-factor values of the first channel tap strongly depends on the UAV altitude, where the value increases from 15.96 dB at altitude 300 m to 17.23 dB at altitude 800 m. For channel taps with larger delay, the K-factor values only slightly depend on the altitude. Similar observations were reported in reference [40]. Therefore, the height of the UAV can be appropriately raised to increase the K-factor value, thereby improving the signal quality and stability of the UAV communication system, making the communication link more reliable. Additionally, it is noted that the Weibull distribution is found to be the best candidate among considered five theoretical distributions for the first tap at all three UAV altitudes. The obtained shape parameters  $\beta_{w1}$  are 1.026, 1.026 and 1.020 at altitude 300 m, 500 m and 800 m, respectively. The scale parameters  $\Omega_{w1}$  are 11.52, 13.62 and 14.07 at altitude 300 m, 500 m and 800 m, respectively. The result reveals that the scale parameter of the Weibull distribution increases with the UAV altitude. As the altitude of the UAV increases, the probability of presence of LoS path also increases. Under LoS conditions, the direct propagation path between transmitter and receiver is the dominant component in the first tap and signal fading tends to be more stable, with less depth of fading.

#### 4.3. Delay-Doppler Spectrum

The Doppler frequencies at different time instants can be obtained using Equation (2). Given that the receiver is fixed, the Doppler shift can be rewritten as [29]

$$f = -\frac{v_t}{\lambda} \cdot \cos(\varphi) \cdot \cos(\theta), \quad (14)$$

where  $v_t$  is speed of the UAV as listed in Table 2, and  $\varphi$  and  $\theta$  are the azimuth and elevation angles between the velocity vector and propagation direction of the signal, respectively. These two angles are calculated based on their position, which is obtained from the navigational equipment on the receiver and the UAV. Thus, the maximum Doppler frequency  $f_m$  and the Doppler frequency of the LoS component  $f_{los}$  for each flight phases can be calculated by the angle information and the UAV's speed. Figure 6 shows the normalized delay-Doppler spectrum of the considered UAV flight phases from FS1 to FS6.

The UAV descends vertically, as shown in Figure 1b, with a speed of 1.2 m/s, which results in a maximum Doppler frequency 10.8 Hz. In such a scenario, the azimuth angle remains nearly constant, whereas the elevation angle changes dramatically resulting in the Doppler frequency of the LoS component within the range between 1.9 Hz and 9.7 Hz. In addition, the steady variation of the UAV can be also observed in the Doppler domain with fewer MPCs, which can be verified in Figure 6a.

Figure 6b shows an example of the averaged Doppler spectrum for low approach scenario, where the UAV flies in from a distance to the takeoff point. The altitude of UAV slowly decreases from 100 m down to 40 m, with speed reduced from 27 m/s down to 1.2 m/s. It can be observed from the Doppler spectrum that there exists diffuse scattered MPCs spreading in delay from approximately 100 ns to 1000 ns, and in Doppler frequency from  $-200$  Hz to 200 Hz.

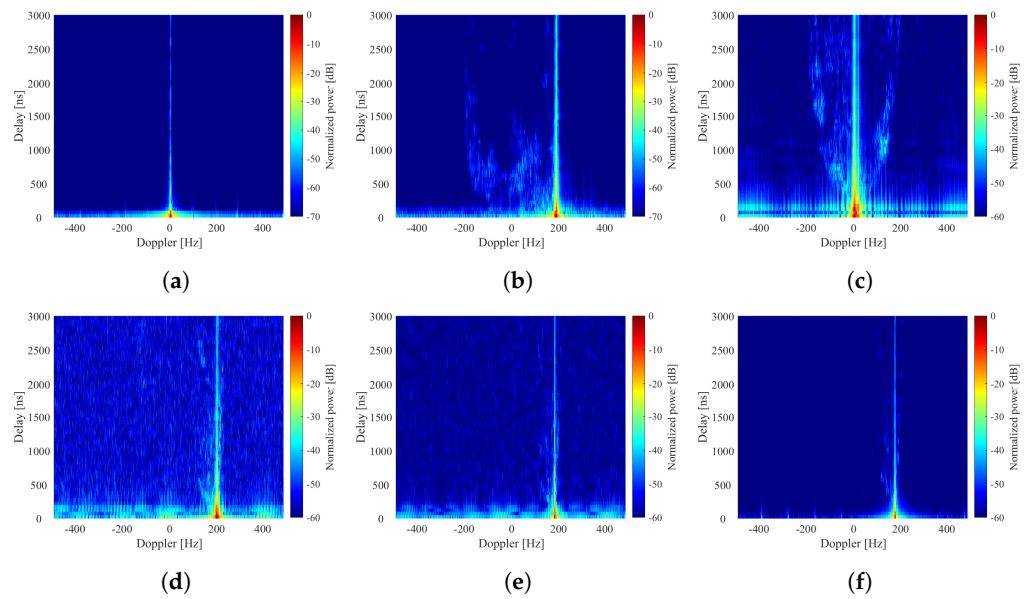


**Figure 6.** Normalized delay-Doppler spectrum. Subfigures (a–f) correspond to the normalized delay-Doppler spectrum of the considered typical UAV flight phases in FS1 to FS6 models.

In scenario FS3, the UAV is within the hovering flight mode, where the UAV speed remains constant at 27 m/s. In this scenario, the Doppler frequency is determined by the angles  $\varphi$  and  $\theta$ . The effective one-dimension (1D) Doppler angle varies from  $0^\circ$  to  $180^\circ$ , resulting in the Doppler frequency from  $-f_{max}$  and  $f_{max}$ . Figure 6c shows the obtained delay-Doppler spectrum at the “inflexion point”, where the distance between UAV and receiver is the minimum within current flight route. As such, the Doppler frequency of the LoS component at this particular instant is 0 Hz. The Doppler frequency of LoS component varies between 89 Hz and  $-152$  Hz, while the UAV travels along the flight route. Similar delay-Doppler spectrum can be found as the first two scenarios, where a typical “U-shape” delay-Doppler spectrum is observed. It indicates the fact that there exists dense scattered MPCs.

In A2G propagation scenarios FS4 to FS6, the propagation environment is expanded from traditional two-dimensional (2D) to three-dimensional (3D), implying that the UAV altitude needs careful attentions. Therefore, we considered in the model the influence of UAV at different altitudes on the Doppler spectrum of A2G channels. Figure 6d–f show the delay-Doppler spectrum for the scenario where the UAV flying steadily along a straight line at altitudes of 300 m, 500 m, and 800 m, respectively. With the increase in UAV altitude, the MPC caused by ground reflection and scattering becomes less dominant. In the meanwhile, the LoS path is less effected by ground objects and becomes dominant, as also reported in [34]. In addition, the Doppler shift of the LoS component remains constant at approximately 201 Hz.

The delay-Doppler spectrum for scenarios FS4 to FS6 show essentially the same variation patterns. Thus, we present the normalized averaged Doppler spectrum of the scenarios FS1 to FS4 conditions in Figure 7. The obvious difference between the A2G channel and other channels is that when the UAV is flying at high altitude, its A2G propagation link is not blocked by any obstacles (trees, houses, etc.), the LoS path persists and the relative power of the LoS path is much higher than that of the other multipaths (e.g., scattering, reflection, etc.). Therefore, in an A2G channel, this is usually represented by the presence of only one peak in its Doppler.

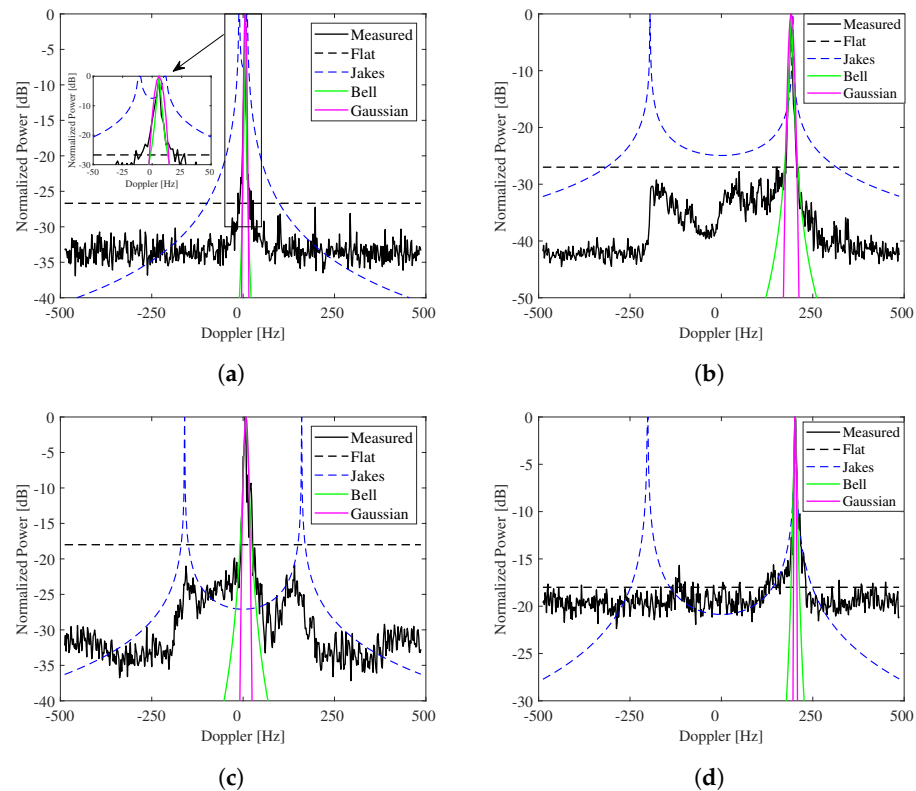


**Figure 7.** The channel model is modeled in typical flight phases of UAV. Subfigures (a–d) are the measured PDF of normalized empirical APDP for FS1 to FS4 models, respectively.

Moreover, it can be observed that in all four considered scenarios, there exists strong Doppler component that is relevant to the first channel tap containing the strong LoS path. In scenario FS1, the maximum power of Doppler spectrum is around 30 dB higher than the rest Doppler components. From the averaged Doppler spectrum, Doppler components caused by MPCs can be also noticed for scenarios FS2 and FS3. It is worth mentioning that the strong Doppler component corresponding to the first tap containing the LoS path is centralized at the Doppler shift frequency according to Equation (14). For all four considered scenarios, the Doppler components corresponding to the first channel taps are significantly stronger than the rest of the components corresponding to other multipath taps. It also confirms the conclusions for the relatively high K-factor values analyzed in the previous section. In addition, the “Jakes”- and “flat”-type spectrum shapes show the poor performance among the four considered spectral distributions, which is consistent with the propagation conditions with the presence of a strong LoS component. The “Bell”- and “Gaussian”-type spectrum shapes fit the LoS component better, especially the “Bell” spectrum with smaller a mean square error. Therefore, we propose to use the “Bell”-type spectrum for modeling the Doppler spectrum at various UAV flight scenarios.

#### 4.4. Doppler Spectrum of Per Tap

As TDL channel model is a “block fading” model, indicating that individual channel taps experience a “quasi-stationary” time variation. In other words, the large-scale parameters of channel are constant, whereas only the virtual movement causes the fast-fading. Therefore, to further model the amplitude variation of each tap in each flight phase, we evaluate the delay-Doppler spectrum of each selected channel taps for all considered scenarios. Figure 6 shows example of the delay-Doppler spectrum for individual scenarios. Considering the noise floor in the Doppler spectrum, we focus on the delay-Doppler spectrum for each tap within the frequency range  $|f| \leq 250$  Hz for a detailed visualization.

In scenario FS1, where the UAV lands vertically, the LoS path is the dominant component with much stronger power than MPCs. As a result, the Doppler spectrum caused by MPC at individual taps are rather weak compared to the first tap that contains the LoS path. Therefore, in this scenario, the Doppler frequency caused by scattering component is very small.

For the FS2 and FS3 scenarios, the broadened Doppler spectrum can be clearly observed especially for channel taps with large delays, which may be caused by the complex terrestrial conditions. Correspondingly, when the UAV flies at a low altitude, e.g., lower than 300 m, a relatively wide spread in the Doppler spectrum can be considered, due to the effect of ground scattering MPC than causes a wide range of Doppler frequencies at different delays. The differences in the Doppler spectra when the UAV is flying at different altitudes (scenarios FS4 to FS6) are relatively small, though that spread in the Doppler spectrum caused by ground MPCs is also noticed.

In addition, we also evaluate the Doppler spectrum for individual channel taps in the considered UAV flight phases. Figure 8 shows the Doppler spectrum of the first channel tap for the scenarios FS1 and FS2, compared with different types of typical spectra. It can be seen that the strongest component is approximately 50 dB higher than the rest Doppler frequency components for scenario FS1 and FS2. The “Bell”-type spectrum shows the best performance among considered spectrum types with minimum error. As such, we propose to use the “Bell”-type spectrum for the first two channel taps, and the “Jakes”-type spectrum for the remaining taps. It is also worth mentioning that Doppler spectrum for channel taps with delay larger than 400 ns is not considered in the model due to very weak power, though that the “U-shape” Doppler spectrum for those taps can be observed in Figures 6 and 7b,c. In addition, the fitted parameter  $A$  of Bell-type spectra are summarized in Table 4.

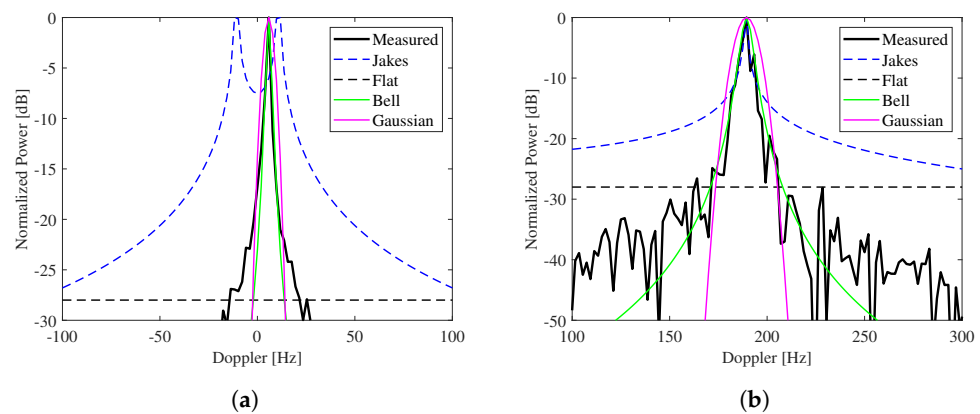


**Figure 8.** The channel model is modeled in typical flight phases of UAV. Subfigures (a,b) are the fitted delay-Doppler spectrum of the first tap in the FS1 and FS2 models.

**Table 4.** Statistic of the proposed TDL model for all considered phases.

Model	Height (m)	Distance (m)	Speed (m/s)	$\tau_{max}$ (ns)	$k_{max}$ (dB)	Tap	$N_m$	Shape	$A$
FS1	0–40	35–60	1.2	400	27.58	9	19537	Bell	23
FS2	40–100	70–300	1.2–27	450	19.78	10	12700	Bell	2231
FS3	100–300	400–600	27	650	20.03	14	10745	Bell	657
FS4	300	1690–2160	27	500	15.96	11	19537	Bell	2200
FS5	500	1740–2170	27	500	17.08	11	19537	Bell	2453
FS6	800	1750–2170	27	500	17.23	11	19537	Bell	2670

#### 4.5. Statistic of the Proposed TDL Model

In the considered rural area scenario, the statistical parameters of the UAV A2G channel are greatly affected by distance between transmitter and receiver, UAV altitude, and velocity. The obtained statistical parameters based on the measurement are listed in Table 4 to demonstrate the dependence of statistical parameters on the impact factors. It can be observed that the K-factor values depends on the UAV altitude and distance. For instance, the K-factor value is the largest at short distance scenario. For the long range Tx-Rx distance scenarios from FS4 to FS6, UAV altitude is the main factor affecting the K-factor values, where the value varies between 15.96 dB and 17.23 dB for altitudes from 300 m up to 800 m. These results also show that the channel dispersion in the time-frequency domain increases with distance and UAV altitude. The resolvable MPCs change as the UAV altitude and distance, as seen from FS2 to FS3. The observable number of MPCs becomes less when the UAV altitude increases, as depicted in Figure 6d,f, which also confirms the conclusions made based on narrowband evaluation [11,34].

## 5. Conclusions

In this paper, we proposed a measurement-based TDL channel model for A2G communication applications in rural areas for different UAV flight phases. Among all of the considered scenarios, a maximum of 14 channel taps with a maximum delay of 650 ns were used in the model. The K-factor value 27.58 dB for the corresponding UAV vertically landing scenario is the largest among all of the considered scenarios. For the high altitude scenarios, the K-factor value increases from 15.96 dB at 300 m to 17.23 dB at 800 m, which also validates the dependence between the K-factor and the UAV altitude. In addition, we analyzed the amplitude distribution characteristics of each tap, where the first tap can be well modeled by Rice and Weibull distributions. Other channel taps can be fitted with a normal distribution. Further, we also evaluate the delay-Doppler spectrum, where we found the LoS component is always the dominant component in considered scenarios. The Doppler spectrum caused by MPC reveals significant differences in different flight phases. In taking-off and landing scenarios, the effect of the MPC on the Doppler spectrum is very small compared to the LoS path. In high altitude scenarios, the Doppler caused by MPC shows dependence on the UAV altitude, where the higher the UAV altitude, the less MPC is observed. In addition, the “Bell”- and “Jakes”-type spectra are used to model the Doppler spectrum for individual channel taps.

**Author Contributions:** Conceptualization, Y.L. and W.W.; funding acquisition, Y.L. and W.W.; investigation, Y.L., Y.H., Z.L., J.Y. and D.S.; methodology, Y.L. and W.W.; software, Y.L. and Y.H.; data acquisition, Y.L., Y.H. and W.W.; supervision, W.W.; validation, Y.L.; writing—original draft, Y.L. and W.W. All authors have read and agreed to the published version of the manuscript.

**Funding:** This work was supported by the National Key Research and Development Program of China under Grant 2020YFB1807001, in part by the Innovation Capability Support Program of Shaanxi under Grant 2022TD-41, the Key Research and Development Program of Xi’an under Grant 24ZDCYJSGG0006, the Natural Science Basic Research Program of Shaanxi under Grant 2023-JC-QN-0686, the National Natural Science Foundation of China under Grant 61871059, and the Joint Fund for Equipment Pre research of the Ministry of Education under Grant 8091B032226. The funder was not involved in the study design, collection, analysis, interpretation of data, the writing of this article or the decision to submit it for publication.

**Data Availability Statement:** The datasets collected and generated in this study are available upon request to the corresponding author.

**Conflicts of Interest:** Junyi Yu is employed by Beijing Metaradio Technologies Co., Ltd. The remaining authors declare that the research was conducted in the absence of any commercial or financial relationships that could be construed as a potential conflict of interest.



## Appendix A. Considered Doppler Spectra

The following algorithms represent the analytical expressions for each Doppler spectrum type. In each case,  $f_d$  denotes the maximum Doppler shift of the associated fading channel system object.

- “Jakes” spectrum

$$P_f(f) = \frac{1}{\pi f_d \sqrt{1 - (f/f_d)^2}}, |f| \leq f_d, \quad (A1)$$

- “Flat” spectrum

$$P_f(f) = \frac{1}{2f_d} \quad (A2)$$

- “Bell” spectrum

$$P_f(f) = \frac{G_b}{1 + A \left( \frac{f-f_d}{f_d} \right)^2}, |f| \leq f_d, \quad (A3)$$

where

$$G_b = \frac{\sqrt{A}}{\pi f_d}. \quad (A4)$$

The coefficient  $A$  can be specified in the dependent field.

- “Gaussian” spectrum

$$P_f(f) = \frac{1}{\sqrt{2\pi\sigma_G^2}} \exp\left(-\frac{(f-f_d)^2}{2\sigma_G^2}\right), \quad (A5)$$

where  $\sigma_G$  is the normalized standard deviation.

## References

1. Mozaffari, M.; Saad, W.; Bennis, M.; Nam, Y.H.; Debbah, M. A Tutorial on UAVs for Wireless Networks: Applications, Challenges, and Open Problems. *IEEE Commun. Surv. Tutor.* **2019**, *21*, 2334–2360. [\[CrossRef\]](#)
2. Menouar, H.; Guvenc, I.; Akkaya, K.; Uluagac, A.S.; Kadri, A.; Tuncer, A. UAV-Enabled Intelligent Transportation Systems for the Smart City: Applications and Challenges. *IEEE Commun. Mag.* **2017**, *55*, 22–28. [\[CrossRef\]](#)
3. Sheng, M.; Zhang, Y.; Liu, J.; Xie, Z.; Quek, T.Q.S.; Li, J. Enabling Integrated Access and Backhaul in Dynamic Aerial-Terrestrial Networks for Coverage Enhancement. *IEEE Trans. Wirel. Commun.* **2024**, *23*, 9072–9084. [\[CrossRef\]](#)
4. Khuwaja, A.A.; Chen, Y.; Zhao, N.; Alouini, M.S.; Dobbins, P. A Survey of Channel Modeling for UAV Communications. *IEEE Commun. Surv. Tutor.* **2018**, *20*, 2804–2821. [\[CrossRef\]](#)
5. Khawaja, W.; Guvenc, I.; Matolak, D.W.; Fiebig, U.C.; Schneckenburger, N. A Survey of Air-to-Ground Propagation Channel Modeling for Unmanned Aerial Vehicles. *IEEE Commun. Surv. Tutor.* **2019**, *21*, 2361–2391. [\[CrossRef\]](#)
6. Zeng, Y.; Zhang, R.; Lim, T.J. Wireless communications with unmanned aerial vehicles: Opportunities and challenges. *IEEE Commun. Mag.* **2016**, *54*, 36–42. [\[CrossRef\]](#)
7. Mao, K.; Zhu, Q.; Wang, C.X.; Ye, X.; Gomez-Ponce, J.; Cai, X.; Miao, Y.; Cui, Z.; Wu, Q.; Fan, W. A Survey on Channel Sounding Technologies and Measurements for UAV-Assisted Communications. *IEEE Trans. Instrum. Meas.* **2024**, *73*, 8004624. [\[CrossRef\]](#)
8. Mao, K.; Zhu, Q.; Qiu, Y.; Liu, X.; Song, M.; Fan, W.; Kokkeler, A.B.J.; Miao, Y. A UAV-Aided Real-Time Channel Sounder for Highly Dynamic Nonstationary A2G Scenarios. *IEEE Trans. Instrum. Meas.* **2023**, *72*, 1–15. [\[CrossRef\]](#)
9. Ni, H.; Zhu, Q.; Hua, B.; Mao, K.; Pan, Y.; Ali, F.; Zhong, W.; Chen, X. Path Loss and Shadowing for UAV-to-Ground UWB Channels Incorporating the Effects of Built-Up Areas and Airframe. *IEEE Trans. Intell. Transp. Syst.* **2024**. [\[CrossRef\]](#)
10. Lyu, Y.; Wang, W.; Sun, Y.; Yue, H.; Chai, J. Low-Altitude UAV Air-to-Ground Multilink Channel Modeling and Analysis at 2.4 and 5.9 GHz. *IEEE Antennas Wirel. Propag. Lett.* **2023**, *22*, 2135–2139. [\[CrossRef\]](#)
11. Lyu, Y.; Wang, W.; Sun, Y.; Rashdan, I. Measurement-based fading characteristics analysis and modeling of UAV to vehicles channel. *Veh. Commun.* **2024**, *45*, 100707. [10.1016/j.vehcom.2023.100707](#) [\[CrossRef\]](#)
12. Lv, Y.; Wang, Y.; Chai, J.; Wang, W. Ultra Wideband Channel Measurement and Analysis for Low Altitude UAV Air-to-Ground Scenario. In Proceedings of the 2021 13th International Symposium on Antennas, Propagation and EM Theory (ISAPE), Zhuhai, China, 1–4 December 2021; Volume 1, pp. 1–3. [\[CrossRef\]](#)
13. Cui, Z.; Briso-Rodríguez, C.; Guan, K.; Zhong, Z.; Quitin, F. Multi-Frequency Air-to-Ground Channel Measurements and Analysis for UAV Communication System. *IEEE Access* **2020**, *8*, 110565–110574. [\[CrossRef\]](#)

14. Sun, R.; Matolak, D.W.; Rayess, W. Air-Ground Channel Characterization for Unmanned Aircraft Systems—Part IV: Airframe Shadowing. *IEEE Trans. Veh. Technol.* **2017**, *66*, 7643–7652. [[CrossRef](#)]
15. Khawaja, W.; Ozdemir, O.; Erden, F.; Guvenc, I.; Matolak, D.W. Ultra-Wideband Air-to-Ground Propagation Channel Characterization in an Open Area. *IEEE Trans. Aerosp. Electron. Syst.* **2020**, *56*, 4533–4555. [[CrossRef](#)] [[PubMed](#)]
16. Cui, Z.; Briso-Rodríguez, C.; Guan, K.; Güvenç, İ.; Zhong, Z. Wideband Air-to-Ground Channel Characterization for Multiple Propagation Environments. *IEEE Antennas Wirel. Propag. Lett.* **2020**, *19*, 1634–1638. [[CrossRef](#)]
17. Cai, X.; Izydorczyk, T.; Jose, R.P.; Kovacs, I.Z. Empirical Low-Altitude Air-to-Ground Spatial Channel Characterization for Cellular Networks Connectivity. *IEEE J. Sel. Areas Commun.* **2021**, *39*, 2975–2991. [[CrossRef](#)]
18. Lim, K.; Kim, H.; Hong, T.C.; Ahn, J.Y. Wideband Transmission for Unmanned Aircraft Systems. In Proceedings of the 2018 International Conference on Information and Communication Technology Convergence (ICTC), Jeju, Republic of Korea, 17–19 October 2018; pp. 1518–1520. [[CrossRef](#)]
19. Schneckenburger, N.; Jost, T.; Walter, M.; Del Galdo, G.; Matolak, D.W.; Fiebig, U.C. Wideband Air-Ground Channel Model for a Regional Airport Environment. *IEEE Trans. Veh. Technol.* **2019**, *68*, 6243–6256. [[CrossRef](#)]
20. Sun, R.; Matolak, D.W. Air-Ground Channel Characterization for Unmanned Aircraft Systems Part II: Hilly and Mountainous Settings. *IEEE Trans. Veh. Technol.* **2017**, *66*, 1913–1925. [[CrossRef](#)]
21. Matolak, D.W.; Sun, R. Air-Ground Channel Characterization for Unmanned Aircraft Systems—Part III: The Suburban and Near-Urban Environments. *IEEE Trans. Veh. Technol.* **2017**, *66*, 6607–6618. [[CrossRef](#)]
22. Matolak, D.W.; Sun, R. Air-Ground Channel Characterization for Unmanned Aircraft Systems—Part I: Methods, Measurements, and Models for Over-Water Settings. *IEEE Trans. Veh. Technol.* **2017**, *66*, 26–44. [[CrossRef](#)]
23. Huang, Q.; An, H.; Guan, K.; Li, Y.; Fei, D.; Zhu, F.; Wang, H. Measurement-based Tapped Delay Line Channel Modeling for Inter-UAV Communications with Typical UAV Attitudes. In Proceedings of the 2022 IEEE 5th International Conference on Electronic Information and Communication Technology (ICEICT), Hefei, China, 21–23 August 2022; pp. 421–426. [[CrossRef](#)]
24. Molisch, A.F. *Wireless Communications*, 2nd ed.; Wiley: Hoboken, NJ, USA, 2015.
25. Rappaport, T. *Wireless Communications: Principles and Practices*; Prentice Hall: Englewood Cliffs, NJ, USA, 1999.
26. Bigñotte, E.M.; Unterhuber, P.; Gómez, A.A.; Sand, S.; Errasti, M.M. Measurement Based Tapped Delay Line Model for Train-to-Train Communications. *IEEE Trans. Veh. Technol.* **2023**, *72*, 4168–4181. [[CrossRef](#)]
27. Acosta, G.; Ingram, M. Model development for the wideband expressway vehicle-to-vehicle 2.4 GHz channel. In Proceedings of the IEEE Wireless Communications and Networking Conference (WCNC 2006), Las Vegas, NV, USA, 3–6 April 2006; Volume 3, pp. 1283–1288. [[CrossRef](#)]
28. Unterhuber, P.; Walter, M.; Fiebig, U.C.; Kürner, T. Stochastic Channel Parameters for Train-to-Train Communications. *IEEE Open J. Antennas Propag.* **2021**, *2*, 778–792. [[CrossRef](#)]
29. Kivinen, J.; Zhao, X.; Vainikainen, P. Empirical characterization of wideband indoor radio channel at 5.3 GHz. *IEEE Trans. Antennas Propag.* **2001**, *49*, 1192–1203. [[CrossRef](#)]
30. Acosta-Marum, G. Measurement, Modeling, and OFDM Synchronization for the Wideband Mobile-to-Mobile Channel. *Georgia Tech Theses*, 2007. Available online: <https://smartech.gatech.edu/handle/1853/14535> (accessed on 20 July 2024).
31. Mohr, W. Wideband Mobile Radio Channels Based on Propagation Measurements. In Proceedings of the 6th International Symposium on Personal, Indoor and Mobile Radio Communications, Toronto, ON, Canada, 27–29 September 1995; Volume 6, pp. 397–401.
32. Simon, M.K.; Alouini, M.-S. *Digital Communication over Fading Channels: A Unified Approach to Performance Analysis*; John Wiley & Sons, Inc.: Hoboken, NJ, USA, 2000.
33. Taricco, G. On the Convergence of Multipath Fading Channel Gains to the Rayleigh Distribution. *IEEE Wirel. Commun. Lett.* **2015**, *4*, 549–552. [[CrossRef](#)]
34. Lyu, Y.; Wang, W.; Chen, P. Fixed-Wing UAV Based Air-to-Ground Channel Measurement and Modeling at 2.7GHz in Rural Environment. *IEEE Trans. Antennas Propag.* **2024**. [[CrossRef](#)]
35. Greenstein, L.; Michelson, D.; Erceg, V. Moment-method estimation of the Ricean K-factor. *IEEE Commun. Lett.* **1999**, *3*, 175–176. [[CrossRef](#)]
36. Sagias, N.; Karagiannidis, G. Gaussian class multivariate Weibull distributions: Theory and applications in fading channels. *IEEE Trans. Inf. Theory* **2005**, *51*, 3608–3619. [[CrossRef](#)]
37. Walter, M.; Shutin, D.; Schmidhammer, M.; Matolak, D.W.; Zajic, A. Geometric Analysis of the Doppler Frequency for General Non-Stationary 3D Mobile-to-Mobile Channels Based on Prolate Spheroidal Coordinates. *IEEE Trans. Veh. Technol.* **2020**, *69*, 10419–10434. [[CrossRef](#)]
38. Walter, M.; Shutin, D.; Matolak, D.W.; Schneckenburger, N.; Wiedemann, T.; Dammann, A. Analysis of Non-Stationary 3D Air-to-Air Channels Using the Theory of Algebraic Curves. *IEEE Trans. Wirel. Commun.* **2019**, *18*, 3767–3780. [[CrossRef](#)]

39. Abdi, A.; Kaveh, M. A Comparative Study of Two Shadow Fading Models in Ultrawideband and Other Wireless Systems. *IEEE Trans. Wirel. Commun.* **2011**, *10*, 1428–1434. [[CrossRef](#)]
40. Cai, X.; Rodríguez-Piñero, J.; Yin, X.; Wang, N.; Ai, B.; Pedersen, G.F.; Yuste, A.P. An Empirical Air-to-Ground Channel Model Based on Passive Measurements in LTE. *IEEE Trans. Veh. Technol.* **2019**, *68*, 1140–1154. [[CrossRef](#)]

**Disclaimer/Publisher’s Note:** The statements, opinions and data contained in all publications are solely those of the individual author(s) and contributor(s) and not of MDPI and/or the editor(s). MDPI and/or the editor(s) disclaim responsibility for any injury to people or property resulting from any ideas, methods, instructions or products referred to in the content.